Kinetic Monte Carlo Study of the Effects of Hydrogen on the 3-d Epitaxial Growth of Ni(100) and Ni(110)

Kenneth Haug* and Jessica Jamoury

Department of Chemistry, Lafayette College, Easton, Pennsylvania 18042

Received: August 20, 2002

The effects of hydrogen on Ni(100) and Ni(110) homoepitaxy, up to 0.7 and 1.1 monolayers depositions, respectively, have been investigated by kinetic Monte Carlo (KMC) methods used to simulate the surfaces growth. A selection of the set of rate constants for the mobility of adsorbed Ni atoms in various surface island configurations, with and without the presence of a small amount of hydrogen impurity, is also reported on here. On the Ni(100) surface we find that the presence of highly mobile H atoms has measurable effects on the size and shape of the Ni island formation. Without the presence of H, the Ni(100) surface growth shows much more extensive roughening than does the Ni(110) surface, and this difference is traced to the axis asymmetry. With the presence of H atoms, the Ni(100) surface roughness is substantially lessened, showing larger islands and flatter islands. Comparisons are also made to the Ni(110) surface, where layer-by-layer growth dominates with or without the presence of H atoms, which is found to have very modest effects on both island size and roughness. For both the Ni(100) and (110) surfaces, the kinetically determined island morphologies at the sub-to-near monolayer level occur over time periods that are long on the deposition time scale, and therefore the morphology differences can become frozen in place.

I. Introduction

The experimental interest in growing thin, smooth metallic films has led to a theoretical effort in understanding microscopic growth and mobility mechanisms involved in metallic films.[1−29] The growth of metallic films can be described in terms of the competition of the rates for various processes involved: the deposition rate, the mobility rate of a lone adatom across a surface, the condensation of a lone adatom with other adatoms to form islands, the evaporation of such islands as lone adatoms break off, and the peripheral diffusion of atoms along the edge of an island.

A question of additional importance in the growth process is what role impurities play in the competition of rates described above. Some experimental reports have noted that impurities can help to induce the layer-by-layer growth of a metal film in some cases and hinder the layer-by-layer growth in other cases.[20−26] For example, nearly twenty years ago, Tung and Graham[20] reported that H hinders W self-diffusion on W(321) but enhances Ni self-diffusion on Ni(110), and the self-diffusion rates are an important component in governing layer-by-layer growth. A very brief sampling of other reports indicates, for example, that oxygen preadsorption induces layer-by-layer 2-d growth in Pt(111) epitaxy,[22] that Sb induces layer-by-layer growth of Ag(111),[23] and that H induces layer-by-layer growth of Cu(100).[1] Because various mechanisms can occur for these processes, the causes and effects are not always obvious. For example, in two of the cases just mentioned in which an impurity enhanced the layer-by-layer growth of a metal, the work of Esch et al.[22] suggested that the cause was oxygen impurity enhancing the mobility of the Pt metal at steps, and the work of Vrijmoeth et al.[23] suggested that the cause was that the Sb impurity was pinning the Ag metal adatoms in place.

In some of our own previous work,[2] we have found that the presence of H on Ni(100) in 2-d studies of the Ni epitaxial growth catalyzes the mobility of lone Ni adatoms across the surface, resulting in accelerated island formation on time scales of the deposition itself. As part of the continuing interest in understanding step-dynamics and 3-d island growth,[27−29] we have also examined how H can catalyze the Erlich−Schwoebel step-edge barriers that govern 2-d versus 3-d island formation.[3] One issue that remains to be determined is how the competition between those two processes play out in terms of net surface roughening versus layer-by-layer growth: the presence of H atoms accelerate island formation during epitaxy, which leads to an increased number of second-layer or higher depositions (adding to 3-d structure); the presence of H also speeds the mobility of the second-layer adatoms toward one another (to stabilize the 3-d structure), but the presence of H atoms also speeds the second-layer Ni toward step edges where H also catalyzes the step-down process (destabilizing 3-d structures and enhancing layer-by-layer growth). A second remaining issue of interest is the effect of surface type, for example the (100) versus the (110) face, on the above-noted processes.

In this paper we report computational kinetic Monte Carlo (KMC) experiments that examine the issues in the previous paragraph. In particular, we study the effect of adsorbed hydrogen atoms, as a low concentration impurity, on the epitaxial growth of Ni on the (100) and (110) Ni faces and we consider both 2-d and 3-d island formation during the epitaxial process. We desire to understand the consequences on the resulting island growth patterns, as effected by the presence of the hydrogen impurity. To carry out the KMC simulations reported here, a more extensive set of rate constants for Ni mobilities were needed than we previously reported on in ref 3, and some of the most important of this set are also discussed here. The additional rate constants were determined by the same methods as noted in refs 1−3.

II. Theoretical and Computational Background

Many recent computational studies of adatom diffusion and crystal growth based upon single atom and correlated atom hopping across activation energy barriers have recently been

reported, a partial sampling of which we note in the references.[27-34] Our approach uses the theoretical and computational details that we have described more extensively in refs 1–3, so only a brief summary is given here. We break the computational problem into two parts: the calculation of activation energy barriers to find rate constants, and the Kinetic Monte Carlo (KMC) simulation of the growth process based upon those rate constants.

The movement of an adsorbed Ni from one binding site to another nearest neighbor site occurs with an activation energy, E_{act}, and the rate constant for this hopping process follows from transition state theory (TST) as

$$k = (k_B T/h)(Q^\#/Q) \exp(-E_{act}/k_B T) \approx \\ (k_B T/h) \exp(-E_{act}/k_B T) \quad (1)$$

In eq 1 the factor k_B is Boltzmann's constant, T is the temperature, h is Planck's constant. The vibrational partition function ratio $(Q^\#/Q)$, of the transition state to the reactant configuration, for several Ni hopping events that we examined, is on the order of unity, and we set it equal to unity in the study discussed here. Quantitative errors in E_{act} due to flaws in the potential energy function we are using will tend to swamp the $Q^\#/Q$ term in any case. The rate constant in eq 1 can be converted into a time constant, τ, assigned to a particular activated hopping event by inverting the rate constant determined from eq 1 as

$$\tau = 1/k = (h/k_B T) \exp(+E_{act}/k_B T) \quad (2)$$

The time constants noted below are evaluated at $T = 250$ K, a temperature that has been used in similar epitaxial growth experiments to that envisioned here.[1] The energy model for the Ni and Ni/H system is the embedded-atom method (EAM) potential energy proposed by Daw and Baskes[35] as modified by Wonchoba, Hu, and Truhlar[36a,b] (we used the model that they designate as EAM5). The activation energy barrier heights for the various hopping events are found from calculation of the minimum-energy profile along the reaction path connecting the initial and final configurations, using a restricted total-energy relaxation scheme and damped molecular dynamics until zero-temperature equilibrium positions are found (with details discussed in refs 1 and 2). Details regarding the number of Ni atoms used in the relaxation scheme are given in ref 3.

The kinetic Monte Carlo (KMC) method is a stochastic solution of the master equation,[37] which in our case governs the deposition and growth processes occurring in this system. We follow a KMC procedure discussed in our previous work,[2] which follows that outlined by Lu and Metiu.[38] The KMC results reported here involve simulating the deposition of up to 0.7 monolayer of Ni for the Ni(100) surface and up to 1.1 monolayers for the Ni(110) surface onto initially flat Ni surfaces that have been prepared either with or without a small (0.05 monolayer) precoverage of hydrogen. As the Ni atoms are deposited (at a fixed deposition rate of 500 s/monolayer), the Ni and H atoms diffuse about this surface and a growth pattern emerges. Periodic boundary conditions are used so that if any adatom leaves the surface on one side of the 2-d surface, it will instantaneously reappear on the other side. The simulations use a 2-dimensional surface size of 40 × 40 lattice binding sites in most cases, and in the studies reported here only three layers in the 3-d growth direction were needed. In several simulations we have tested various 2-d surface sizes, for example from 30 × 30 to 50 × 50, to verify that edge effects are not significant (some of these test details are noted in Appendix A). Our

computational algorithm monitors for the number of 3-d surface layers needed in each case, so that if stable third-tier islands are formed, then a fourth 3-d growth layer can be added, etc. The temperature is set at 250 K in all cases.

For the studies reported here k_{ref} is set by an activation energy of 0.40 eV, corresponding to a time constant $\tau = 2.3 \times 10^{-5}$ s as the simulation clock cycle. The choice of the simulation clock cycle is an important one and involves a balance between computational efficiency (a larger clock cycle) and simulation accuracy (a smaller one).[37-39] We therefore have studied this choice in some detail, as discussed further in Appendix B, and the evidence presented there suggests that this reference value does distinguish the important rates that govern the 2-d and 3-d growth patterns we are examining here. A shortcoming of all KMC simulations is that they are blind to any mechanisms not implied in their rate constants. In an attempt to at least minimize this blindness, and to avoid a seemingly ad hoc selection of rate mechanisms, we have defined a systematic choice of rate processes for each surface, which are denoted in section III below. Our KMC simulations also make use of both the forward and reverse rate constants for a given hopping event to build detailed balance into the KMC study.

The key observables followed in the simulation are the island size versus time and the number of second- and third-layer island sizes versus time (where our time scale is set by the deposition rate); lone Ni atoms are *not* counted as an island. We carry out multiple simulations (typically 10–20) of each coverage using different random number seeds to govern the absorption and diffusion events and then average the resulting island size versus time over the simulations. This diminishes the effect of any rare configuration from skewing the results and also allows us to establish statistical confidence limits on the average island size values.

III. Results

We present our results for the Ni(100) and Ni(110) single crystal faces separately in sections 1 and 2 and sections 3 and 4 below. For multifaceted surfaces, the relative binding energy of the H adatoms on each surface can, of course, modify the net results seen. However, for the EAM5 potential energy surface used, the binding energy of H is 2.699 and 2.701 eV, respectively, on the (100) and (110) surfaces. At a temperature of 250 K, this gives slight asymmetry in Boltzmann distribution populations of 0.477 and 0.523 on the (100) and (110) surfaces, respectively.

(1) Ni(100) Activation Energies. For the Ni(100) case, the regime of 2-d (submonolayer) epitaxial growth has been reported previously,[1,2] and we will here only summarize the key results discussed in refs 1 and 2 in greater detail. The H atom prefers the surface 4-fold hollow site and will hop from site-to-site by overcoming a 0.17 eV potential barrier on the bare terrace (at 250 K this gives a time constant from eq 2 of $\tau = 5.1 \times 10^{-10}$ s). It is known experimentally[40-44] that H can occupy bulk interstitial sites and affect surface activity in many metal systems, but experiments at low H surface coverage have also shown that only a small amount of H is needed to substantially modify the growth dynamics of metal surfaces, which suggests that at low converage much of the H is remaining at the surface.[1] In the EAM5 potential used here the H/Ni(100) subsurface site lies 0.41 eV above the open terrace surface binding site, giving a Boltzmann probability weight of 5.1×10^{-9} for the subsurface site compared to the surface site at 250 K. Because in the KMC simulation we distribute H atoms according to Boltzmann probabilities, we therefore avoid the use of subsurface H in the KMC reported below. The Ni adatoms on Ni(100) also prefer
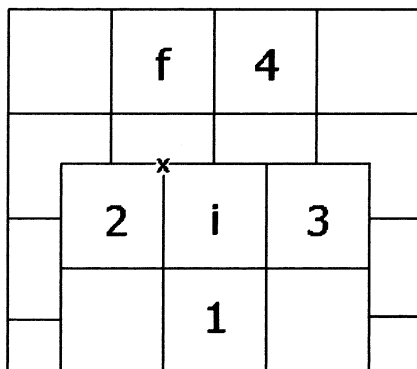
Effects of Hydrogen on Ni(100) and Ni(110) Homoepitaxy

J. Phys. Chem. B, Vol. 106, No. 43, 2002 **11255**

Figure 1. Ni atom site labels for the Ni(100) step-down processes with notation as discussed in the text.

TABLE 1: Sampling of Activation Barrier Energies, *E* (eV), and Time Constants, τ (s) from Eq 2, for Ni(100) Selected Hopping Events Discussed in the Text for the Uncatalyzed Case (uncat) and the H-Catalyzed Case (cat/with H)[a]

	uncat		cat/with H	
	E		*E*	
event on Ni(100)	(eV)	τ (s)	(eV)	τ (s)
3-d straight-edge step-down (direct)[b]	0.95	2.7(+6)	0.67	6.2(+0)
3-d straight-edge step-down (exchange)	0.70	2.5(+1)	0.67	6.2(+0)
3-d corner-site step-down (direct)	0.93	1.1(+6)	0.75	2.5(+2)
3-d corner-site step-down (exchange)	0.71	3.9(+1)	0.68	9.9(+0)
3-d kink-site step-down (direct)[b]	0.70	2.5(+1)	0.61	3.8(−1)
3-d kink-site step-down (exchange)	0.48	9.1(−4)	0.45	2.3(−4)

[a] The values for τ are denoted such that 5.1(−10) is equal to 5.1 × 10^{-10}. [b] The values for these processes were also reported in ref 3.

the 4-fold hollow site, and a lone Ni adatom will hop from site to site by overcoming a 0.61 eV potential barrier ($\tau = 3.8 \times 10^{-1}$ s). During the epitaxial growth, the H atoms act principally as a catalyst, stabilizing the transition state for site-to-site Ni hopping by formation of a Ni−H bond and leaving the reactant configuration and product configuration energy wells at essentially the same level. The physical origin of the effect of H on the Ni can be traced to a weak, transient H−Ni bond that forms during the hopping process, stabilizes the transition state, and is described in great detail in ref 2 and 3. The net result from ref 2 is that the lone-Ni atom's accelerated mobility in the presence of H-atoms is the dominating H-effect on the final surface morphology during 2-d growth. In ref 3 we examined several basic ascending and descending processes by which a Ni adatom steps up or down a surface level, and we found that the presence of H is also acting as a catalyst for these edge barriers, commonly known as Ehrlich−Schwoebel barriers.[45−47]

The KMC simulations for Ni(100) reported below use a more extended and systematic set of 3-d mechanisms than those examined in ref 3 where only uncorrelated (or direct) Ni hops up or down a surface level were noted. Whereas the terrace level Ni adatoms are unlikely to exchange places with a surface atom on the (100) surface (the barrier to such a step is 1.35 eV), layer exchange has been found to be a common pathway at step edges. In this current work, we therefore report correlated hopping events involving two to three Ni atoms at the step edges, which are also used for the KMC simulations. We have examined several direct and exchange pathways for second-tier Ni adatoms to overcome a step-edge barrier and descend from the top of such an island to the terrace level, as summarized in Figure 1 (for straight-edge and kink sites). In Figure 1, the terrace level is represented by the background (in the upper part of the figure) block structure and the first-tier layer is represented by the forward block structure. Site "i" represents the initial location of a second-tier Ni adatom, and other Ni atoms can occupy second-tier sites labeled 1−3 and terrace level site 4 (for a kink-site configuration). Site "f" represents the final target site of a hopping Ni atom, and site "x" locates a Ni atom that is part of the first-tier block structure that participates in exchange processes. In the notation of Figure 1, a Ni adatom residing on the seccond-tier growth level at site "i" jumps to the first-tier level "f" (by pathways noted below). Other Ni adatoms may or may not occupy the surrounding sites labeled 1−4, and a H atom may be present at or on the approach to the target binding site. Figure 1 therefore shows the 16 net configuration changes for step-down processes used in our KMC simulation (with Ni atoms variously occupying sites 1−4), and we have examined each of these configuration changes by a number of mechanisms. For example, in the straight-edge step-

down situations, we have compared a direct path (in Figure 1 notation, i → f, with an activation energy of 0.95 eV), a two-atom exchange path (i → x → f, with an activation energy of 0.70 eV), and a three-atom exchange path (not directly indicated in Figure 1, but it would involve the path i → x → surface−atom → f, with an activation energy of 1.86 eV). Because the KMC simulation is concerned with only the initial and final configurations, only the lowest energy pathway is used in the KMC. Selected activation energies and associated time constants for the direct and 2-atom exchange pathways are noted in Table 1 for typical straight-edge, corner, and kink-site configurations for a lone second-tier adatom. In the table, the energy barrier and the associated time constant are given for each process along with the effect on the barrier and time constant of having a hydrogen atom along the reaction path. (Other selected barriers for Ni mobility on the (100) terrace level are found in ref 3.) In this table, we see that the two-atom exchange paths dominate the direct step-down pathways and also that the effects of H on Ni step-down processes are important for both direct and exchange pathways, and at both the kink and the straight-edge sites. As seen in Table 1, the H atom effects on Ni descending Ehrlich−Schwoebel (step-down) barriers are typically similar to that found for the kink-site exchange process step-down, in which a 0.48 eV barrier is lowered slightly to 0.45 eV due to the H atom stabilization. We can also see that straight-edge and corner step-downs are very similar in barrier height, because they actually proceed by the same mechanism, which we can understand in the following manner. Using Figure 1, position "i" represents a corner if for example position "3" and its underlying support are missing. In this configuration, the corner step-down process via exchange in fact prefers the same pathway (i → x → f) as noted in Figure 1 for the straight-edge process rather than an exchange process with the first-layer corner atom. In testing the KMC model we have therefore found that there is no observational difference if we distinguish the corner versus straight-edge step-down processes or not.

The ascending Ehrlich−Schwoebel (step-up) energy barriers for Ni terrace adatoms onto an island at straight edges, corners, and kinks are on the order of 1 eV and larger and are included in the KMC simulation to maintain a detailed balance (but such moves are rarely encountered and prove to be unimportant as island building steps at the temperature considered here). Whereas the KMC simulation includes 16 step-up processes for detailed balance purposes, in practice we include only 8 distinct step-up rate constants, because the Ni presence at site 4 in Figure 1 effectively kills the step-up process. Also, the H-atom effect on Ni ascending Ehrlich−Schwoebel (step-up) rates, though significant in energy change, is minimal in net effect due to the still large barriers involved (typically over 1.0 eV), as discussed more fully in ref 3.
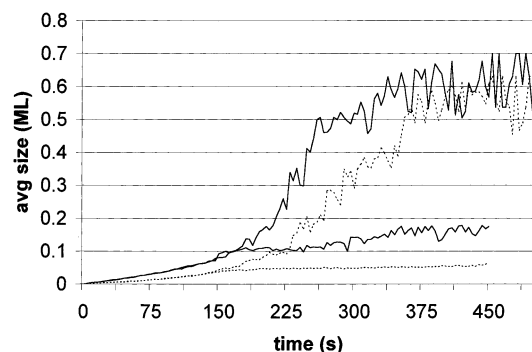
Figure 2. Average Ni island size (in monolayer units) vs time (in seconds) for Ni(100) epitaxy. The upper solid (dashed) curve is for 0.7 monolayer of Ni deposited over the first 350 s with (without) 0.05 monolayer precoverage of H. The lower solid (dashed) curve is for 0.3 monolayer of Ni deposited over the first 150 s with (without) 0.05 monolayer precoverage of H.

Figure 3. Average second-tier Ni island size (in absolute number) vs time (in seconds) for Ni(100) epitaxy. The cases given are for 0.7 monolayer of Ni deposited over the first 350 s both with 0.05 monolayer precoverage of H as a catalyst (solid curve) and without any H (dashed curve).

The barrier values, discussed above, beg an answer to the question of what net effect the hydrogen will have on the growth process. The net result of having H atoms on the surface is difficult to predict from the examination of the energy barrier effects alone due to the competition between conflicting trends, both catalyzed by the presence of H. Hydrogen will increase the rate of first-tier island formation, allowing more second-layer depositions to occur (enhancing roughening of the surface). Hydrogen affects the second-tier Ni adatoms by accelerating them toward second-tier island nucleation events (enhancing roughening), but hydrogen also accelerates Ni toward step-edges and catalyzes the Ni step-down (enhancing layer-by-layer growth). The KMC simulations allow this competition to play out. Our KMC simulations make use of the complete set of 64 uncorrelated single hopping events occurring on the single terrace level (2-d growth), as denoted in Figure 1 of ref 2. This 2-d set of hopping events is extended in the present work for 3-d growth via inclusion of the 24 Ni step-down and step-up mobilities noted above, with and without the presence of hydrogen. This results in a total of 176 rate constants for the KMC simulation on the Ni(100) surface (i.e., 88 rate constants for Ni hops uncatalyzed by hydrogen are supplemented by another 88 rate constants for Ni hops when hydrogen is present).

(2) Ni(100) KMC. In the KMC study for Ni(100), we use the rate constants described above along with a 500 s/monolayer deposition rate. In this study, we find that over the few hundred seconds of typical epitaxial growth, the competition of hopping, evaporation, condensation, and deposition processes will tend to stabilize islands building on rectangular bases, in which second-tier adatoms will more readily step down at a kink site to complete a rectangular base, and more readily reflect back from a straight-edge to maintain that rectangular base, in agreement with $m \times n$ patterns previously emphasized in the literature.[7,12] The numerical results of the competition between the various rate processes are summarized in Figures 2 and 3 for the Ni(100) surface. In Figure 2, the average Ni island size (in monolayer units) vs time (in seconds) for Ni(100) epitaxy is given. The upper solid (dashed) curve is for 0.7 monolayer of Ni deposited over the first 350 s with (without) 0.05 monolayer precoverage of H. The lower solid (dashed) curve is for 0.3 monolayer of Ni deposited over the first 150 s with (without) 0.05 monolayer precoverage of H. The systems then evolve without further deposition for the remaining time noted. The first key feature noted in Figure 2 is that H precoverage accelerates the net growth of islands over the deposition time as we see that the upper solid curve (with H) measuring the average island size in monolayer units rises significantly faster
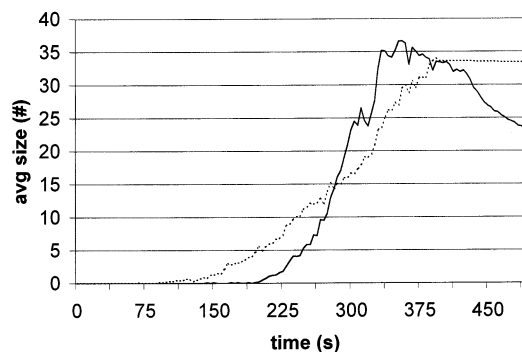
than the upper dashed curve (without H). One of the most notable effects of H as a catalyst is the acceleration of lone Ni atom mobility across the open terrace, and the shape of these curves is primarily the consequence of that.[2] In test calculations of 0.7 monolayer Ni growth in which the 0.05 monolayer H-atom effect on the lone Ni-atom activation energy is suppressed, the two upper curves represented in Figure 2 become essentially indistinguishable. At longer times, in the 400−450 s range, we see that the gap between the curves diminishes, in agreement with the essentially catalytic effect of the hydrogen, and both curves overlap as the surface islands coalesce into a globally connected region with coverage of about 0.6 monolayer. The large fluctuations noted in Figure 2 represent the dynamic nature of the islands, as atoms evaporate and small new islands form and are later absorbed into larger islands. With further KMC simulations averaged into the fold, these fluctuations dampen out, but the trends are quite clear already in Figure 2 (the Monte Carlo standard deviations of the average are approximately identical in magnitude to the fluctuations noted in the figure). If the deposition is stopped at a lower coverage (e.g., 0.3 monolayer as shown by the two lower curves of Figure 2), then the distinction in island size caused by the presence of H (lower solid curve) can be maintained for extended times over the uncatalyzed case (lower dashed curve), as island evaporation and condensation tend to balance.

Our primary interest here is in second-layer growth (surface roughening), which begins in our KMC simulations at around 150−200 s, corresponding to about 0.3 monolayer of Ni deposition. The average second-layer island size versus time is shown in Figure 3 for the 0.7 monolayer deposition both with (solid curve) and without (dashed curve) 0.05 monolayer precoverage of H. Notice that the second-layer island size curves have several different regions of behavior in Figure 3. The first region occurs over about the first 250 s, as the uncatalyzed growth curve rises above the catalyzed growth curve. Recalling from Figure 2 that Ni islands with H present are larger than Ni islands without H, one might expect the opposite behavior because more Ni should be deposited as second-layer atoms. Indeed they are, and in direct proportion to the number of stable second-layer sites, as verified in Figure 4 (in which the top solid curve and the top dashed curve give the number of Ni atoms deposited on the second layer with H and without H, respectively). However, because the presence of H accelerates lone Ni atoms, on the second layer the Ni can be accelerated to either nucleation events forming semistable second-layer islands, or to a step edge where H also catalyzes the step-down process. The other curves in Figure 4 give the number of Ni atoms
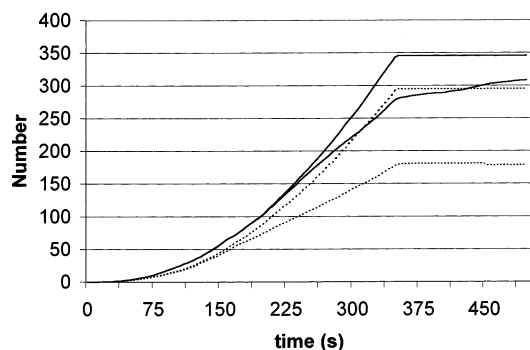
Effects of Hydrogen on Ni(100) and Ni(110) Homoepitaxy

J. Phys. Chem. B, Vol. 106, No. 43, 2002 **11257**

Figure 4. For the 0.7 monolayer Ni cases noted in Figure 3: (top solid curve and top dashed curve) the number of Ni atoms deposited on the second layer with and without H, respectively; (lower solid curve and lower dashed curve) the number of Ni atoms stepping down from the second layer to the terrace with and without H, respectively.

stepping down from the second level to the terrace level when H is present (lower solid) and when H is not present (lower dashed). Notice that for about the first 225 s, essentially all Ni deposited on the second layer step down to the terrace level in the catalyzed case (solid), whereas in the uncatalyzed case (dashed) the divergence of the deposition and step-down curves begins much earlier, at about 150 s. This point of divergence of the deposition and step-down curves represents the nucleation of stable second-layer islands, as seen in the first region of Figure 3. In the second region of Figure 3 (roughly 250−350 s), we are now at a point in time in which stable second-layer islands have been formed in both the H and non-H cases. Just as in initial first-layer growth, as noted in Figure 2, the H acceleration of lone Ni atom mobility allows for larger islands to form (now on the second layer, roughening the surface). However, at times greater than 350 s in Figure 3 (the third region) we find a new distinction from first-layer growth. The second-layer islands in the presence of H are not as stable as in the absence of H because evaporation is still weakly catalyzed (see ref 2 and 3). For an evaporated second-layer Ni, the Ni can either rejoin another second-layer island with no net effect on roughening or move to a step edge and step down. In first-layer growth, of course, the evaporated island atoms can only rejoin an island after wandering about for a time, and stabilization of the average island size is seen (as in the dashed curves of Figure 2). In Figure 4, we monitor this continued slow step-down of Ni atoms from the second layer in the presence of H (the lower solid curve which shows a slow rise from 350 to 500 s), as opposed to the more stable case without H (the nearly constant lower dashed curve).

As representative samples of the surface growth pattern, "snapshot" images are given in Figure 5 for first-layer growth at the 0.3 monolayer coverage, and in Figure 6 for second-layer growth at the 0.7 monolayer coverage. Both figures give patterns with (a) and without (b) H-atom catalysis on a 40 × 40 grid with periodic boundary conditions. The images correspond to the data given in Figure 3; it is taken at the final time point and for clarity shows only the second-tier layer Ni atoms for the 0.7 monolayer deposition. The *m* x *n* pattern previously reported, for example, in 2-D cluster experiments on Ag(100)[7] and, in theory,[12] is clearly suggested here, although our islands are still evolving slowly and a number of kinks are still apparent. Also the average island size and island number distinction between the H-catalyzed and uncatalyzed cases for the different layers, as discussed above, is clearly apparent as well. In first-tier growth, the H-catalyzed case (Figure 5a) shows fewer islands (3 vs 5) of larger average size (160 vs 96 atoms or 0.06 vs 0.10
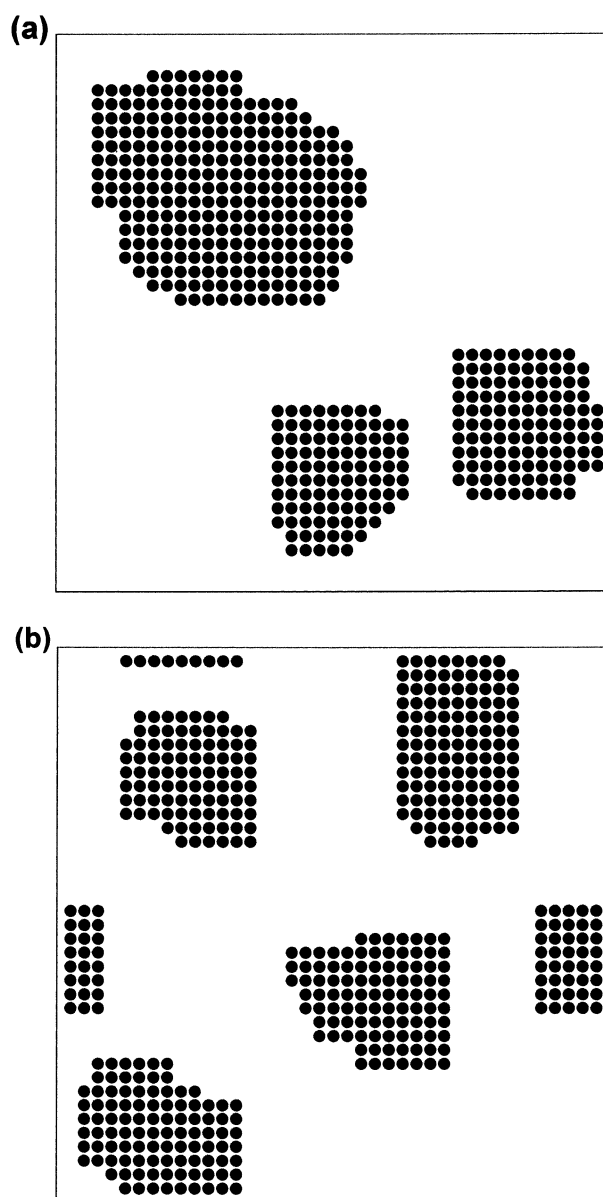

Figure 5. Typical sample of the first-layer growth pattern on Ni(100) at the 0.3 monolayer coverage with (a) and without (b) H-atom catalysis on a 40 × 40 grid with periodic boundary conditions. The images corresponding to the data given in Figure 3 taken at the final time point and only the Ni atoms are shown.

monolayer) than the uncatalyzed case (Figure 5b), in good agreement with the lower curves of Figure 3, which is also in agreement with the experimental results for the somewhat similar Cu(100) surface in which a submonolayer deposition of Cu was seen to form islands of increased size in the presence of hydrogen impurity.[1] Note that for the reasons discussed above, the second-tier pattern in Figure 6 is not simply a rerun of the first-tier layer in Figure 5. That is, we are not seeing near-perfect layer-by-layer growth, which we want to note now for comparison to the Ni(110) surface discussed below. We do see in Figure 6 that the second-tier H-catalyzed case (a) shows fewer islands (2 vs 4), but of smaller average size (23 vs 38 atoms) than the uncatalyzed case (b), which is in very good agreement with the upper curves of Figure 3.

(3) Ni(110) Activation Energies. The Ni(110) surface is characterized by two length scales, noted here as the long axis (of 3.52 Å) and the short axis (of 2.49 Å). Some important aspects of Ni and H on this surface have been reported in ref 3
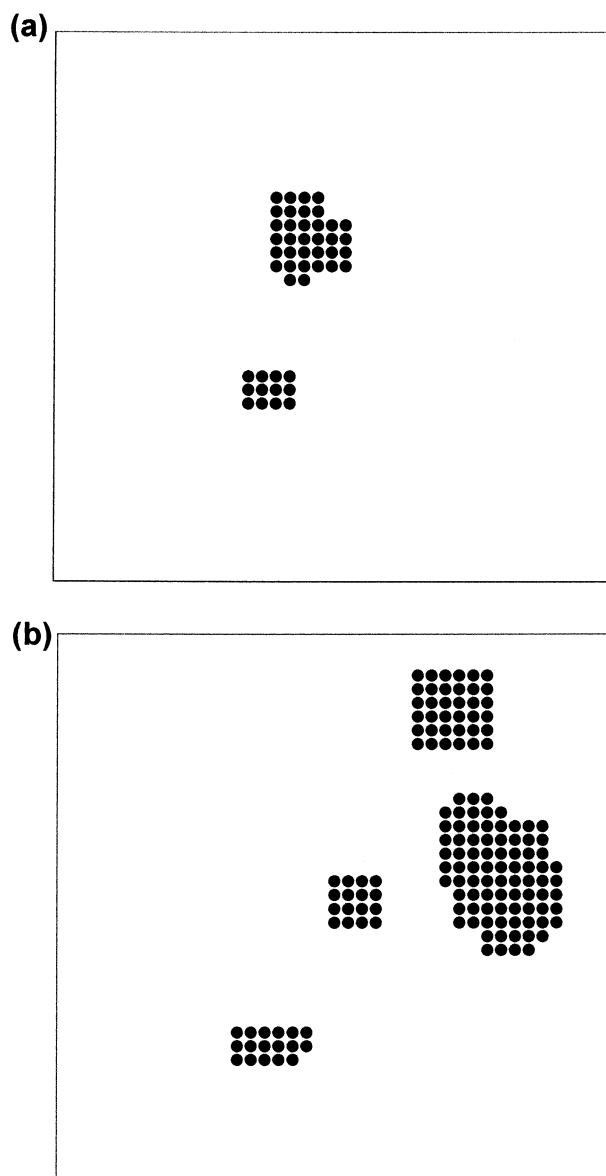
(a)

(b)

Figure 6. Typical sample of the second-layer growth pattern on Ni-(100) at the 0.7 monolayer coverage with (a) and without (b) H-atom catalysis on a 40 × 40 grid with periodic boundary conditions. The images corresponding to the data given in Figure 3 taken at the final time point and only the Ni atoms are shown.

and will be summarized here. The H atoms will hop from cell-to-cell along the Ni short axis by overcoming a 0.013 eV potential barrier, and along the Ni long axis by overcoming a 0.18 eV barrier. The H-atom can also sit in several subsurface interstitial sites, but the most stable site in the first subsurface level lies 0.395 eV higher in energy than the stable surface site, giving a relative Boltzmann probability of 1.0×10^{-8} at 250 K. Therefore, as with the (100) surface, we have not accounted for subsurface H in our KMC study. The Ni adatoms on Ni-(110) reside in the symmetric hollow site and the asymmetry of the surface results in Ni–Ni dimer bonding on the terrace level, which is substantially stronger along the short (−0.320 eV) than the long axis (−0.035 eV). As discussed in the KMC simulation section below, these energy differences give rise to the characteristic long, thin island formation at submonolayer coverages, which are seen in our KMC simulation below, as well as in Ag(110) and Cu(110) cases from the literature.[48,49] An alternative source of the characteristic island shape could have been a difference in mobilities along the two axes. In fact,
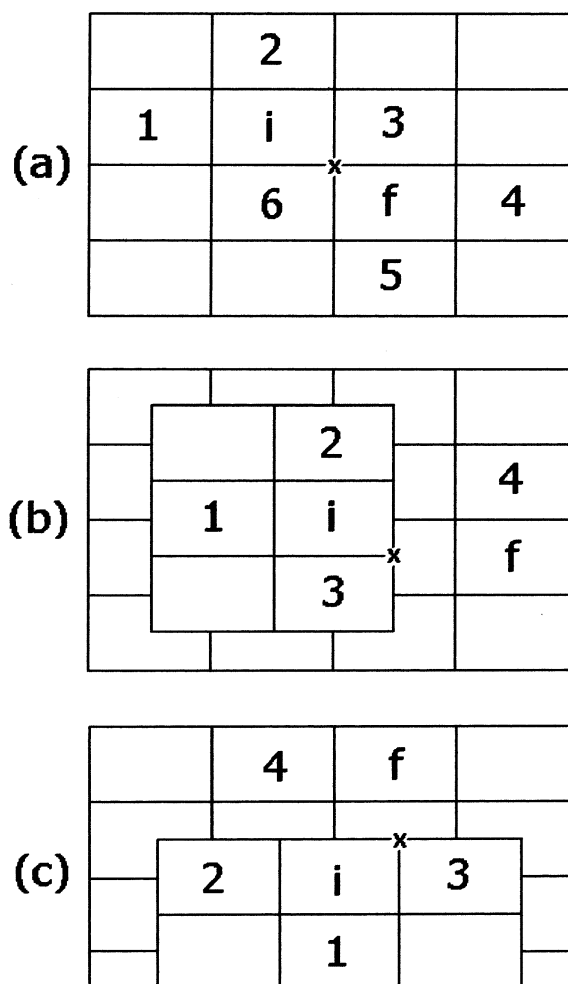
(a)

(b)

(c)

Figure 7. Ni atom binding site labels denoting hopping processes on Ni(110) with notation as discussed in the text. Site labels for Ni(110) terrace level mobility in the generalized long-axis direction are given in (a). Site labels for step-down processes for the long-axis direction are given in (b), and for the short-axis direction in (c).

however, the Ni mobility on the terrace level occurs by an adatom–surface exchange process,[50,51] which mixes the short and long axis mobilities, and the net result is that mobilities in both directions are on about the same time scale. Also discussed in detail in ref 3 is the very weak catalytic nature of hydrogen on Ni/Ni(110) mobility both on the terrace barriers and on the Ehrlich–Schwoebel barriers at step edges, predicting little net effect of H on the Ni(110) growth patterns.

The KMC simulations reported below use a total of 224 uncatalyzed rate constants (supplemented by 224 hydrogen-catalyzed ones), a more extended and systematic set of barriers than those noted in ref 3. On the terrace level, we use a set of 64 rate constants for the uncatalyzed Ni hopping along the short axis (supplemented by 64 catalyzed rate constants) that correspond to those schematically represented in Figure 1 of ref 2, now for the (110) surface. Another set of 64 terrace-level rate constants for the uncatalyzed Ni hopping along the long axis (supplemented by 64 catalyzed rate constants) correspond to those schematically represented in Figure 7a, in which an adatom initially at site "i" moves via surface exchange (i → x → f) to site "f". Sites labeled 1−6 denote different configurations, depending on if a Ni adatom is or is not present at each site in the 64 different combinations, and site "x" is a surface atom participating in the exchange process. The symmetry partners of the process noted in Figure 7a, for example, in which the

Effects of Hydrogen on Ni(100) and Ni(110) Homoepitaxy

J. Phys. Chem. B, Vol. 106, No. 43, 2002 **11259**

TABLE 2: Sampling of Activation Barrier Energies, E (eV), and Time Constants, τ (s) from Eq 2, for Selected Ni(110) Exchange-Hopping Events Discussed in the Text[a]

Ni (110) event	short axis		exchange (long axis*)	
	E (eV)	τ (s)	E (eV)	τ (s)
3-d straight-edge step-down	0.72	6.3(+1)	0.78	1.0(+3)
3-d straight-edge step-down (cat)	0.69	1.6(+1)	0.76	4.0(+2)
3-d corner-site step-down	0.68	9.9(+0)	0.73	9.9(+1)
3-d corner-site step-down (cat)	0.65	2.4(+0)	0.71	4.0(+1)
3-d kink-site step-down	0.47	5.7(−4)	0.53	9.3(−3)
3-d kink-site step-down (cat)	0.46	3.6(−4)	0.53	9.3(−3)

[a] The values for τ are denoted such that 3.0(−13) is equal to 3.0 × 10^{-13}, and H-catalyzed processes are denoted by (cat).

adatom moves upward rather than downward, etc., are of course also included in the KMC simulation.

The KMC simulation also includes 48 step-down uncatalyzed step-edge hopping processes (supplemented by 48 catalyzed along with their detailed balance step-up partners), a few of which we will discuss here in more detail. For example, the step-up and step-down Ehrlich−Schwoebel barriers for Ni determining the reflectivity of step edges on the (110) surface is governed by direct hopping processes along the short axis and by adatom−surface exchange processes along the long axis. A schematic representation of the step-edge processes used in our KMC simulation for downward steps is given in Figure 7b,c. Both straight-edge and kink-site processes are represented in Figure 7 by appropriate occupancy of the numerically labeled sites with Ni atoms. In Figure 7b,c, the terrace level is represented by the larger background block structure and the first-tier island layer is represented by the smaller forward block structure. Site "i" represents the initial location of a second-tier Ni adatom, and other Ni atoms can occupy second-tier sites labeled 1−3 and terrace level site 4. Site "f" represents the final target site of a hopping Ni atom, and site "x" locates a Ni atom that is part of the first-layer island structure that is tested for participation in exchange processes. In long-axis and short-axis step-downs we have tested both direct (i → f), one-atom exchange (i → x → f), and two-atom exchange (i → x → terrace atom → f) processes. In Table 2, selected entries of step-down energy barriers for corner sites, straight-edge sites, and kink sites are given for a lone second-tier adatom starting configuration. Further examples of (110) barriers on the terrace level can be found in ref 3. Two points to note for the step-down barriers listed in Table 2 are the small effect of hydrogen as a catalyst and the dominance of kink-site locations for adatom step-down (this last point similar to that seen on the 100 surface). For example, when a second-tier adatom steps to the terrace level at a short-axis kink site, the direct hopping pathway (as noted by i→f in Figure 7c) dominates, and the step-down pathway has a barrier of 0.47 eV (without H catalysis), dropping to 0.46 eV with H at the activated target site. We have examined the effect of an H atom at many locations in the reaction path zone and this position gives the most significant effect. The rationale for this weak catalytic effect is the same as that discussed fully in ref 3: briefly, the low H-mobility barriers diminish the transition state Ni−H "dimer" bond. For the long-axis step-down at a kink site, a second-tier to first-tier exchange process dominates (as noted by i → x → f in Figure 7b) with an energy barrier of 0.53 eV, which is essentially unaffected by the H presence. Other competing kink-site pathways governing step edges have similar or higher energy barriers. For example, the two-atom concerted motion of a second-tier adatom exchanging with a first-tier adatom along the short axis has a barrier of 0.70 eV (without H), and the three-atom concerted motion of a second-tier adatom exchanging with a first-tier adatom at the island corner while that first-tier adatom exchanges with a terrace-level surface atom has a barrier of 0.76 eV (without H). The direct long-axis step-down of a second-tier adatom to the terrace level has an energy barrier of 1.32 eV (without H). We have also tested a wide variety of pathways at straight-edge and corner sites and Table 2 gives only the lowest energy barriers. Because the final configurations of the various step-down pathways (at straight-edge, corner, and kink sites) are either exactly the same or very similar, only the lowest barrier for each site is used in our KMC simulation.

The Ni adatom step-up mobility on the (110) surface is similar to that seen on the (100) surface: significant energy barrier lowering but still leaving very high barriers. For example, the long-axis step-up barrier for Ni, proceeding by an exchange process reversing that noted by i → x → f in Figure 7b, is 0.97 eV, and lowers to 0.74 eV by the presence of hydrogen at the top of the step (but this catalyzed barrier still results in a time constant of 155 s and is therefore rarely seen in the KMC simulations noted below).

The net result of the step-down pathways on 3-d features formed during Ni(110) epitaxial growth will be confirmed by the KMC studies, but we can already anticipate the pattern from the barriers noted in Table 2. A second-tier lone atom will be very mobile along the top of the long narrow first-tier islands and will have a reasonable step-down propensity only at kink sites. Unlike the Ni(100) surface with its equivalent $x−y$ axis growth and dominance of kink-site step-down mobility, the kink-sites on the (110) surface do not quickly "heal" themselves into a rectangular configuration. On the (110) surface, the kink instead will propagate along the island and result in widening the island by one lattice unit (e.g., long 2-atom wide islands become long 3-atom wide islands, etc.).

(4) Ni(110) KMC. In the KMC study for Ni(110), we use the rate constants described above along with a 500 s/monolayer deposition rate. The KMC simulations on the Ni(110) surface, presented in Figures 6 and 7, are characterized by 2-d layer-by-layer growth, with the presence of hydrogen having only modest effects as predicted above, and as Figure 6 and Figure 7 indicate. The growth pattern maintains the asymmetry of the underlying lattice: rapid growth in the short-axis direction as compared to the long-axis direction. The initial surface structure is therefore dominated by long, thin islands that widen as the deposition continues, as also reported in the Ag(110) and Cu-(110) systems.[48,49] The dynamics of this asymmetry is not strongly dependent on the lone Ni atom mobility, because the surface exchange mechanism noted above gives approximate equality to mobility of lone atoms in either direction. The dynamics of the asymmetry is instead governed by the stronger site-to-site binding energy along the short vs long axis, which manifest in the KMC simulation as the relative activation energies for forming/breaking bonds in either direction. As a confirmation test of this concept, we find that when the lone atom hopping rates for the two directions are equalized, the long thin island patterns still appear, but when the condensation/evaporation rates in the two directions are equalized with the hopping rates remaining asymmetric, the block island patterns reminiscent of the (100) surface growth appear.

These growth features show up in Figure 8, which gives the average island size in monolayer units, and Figure 9, which gives the absolute island size for second-tier islands, for both the uncatalyzed growth process (dashed line) and the catalyzed process with 0.05 monolayer of hydrogen precoverage (solid
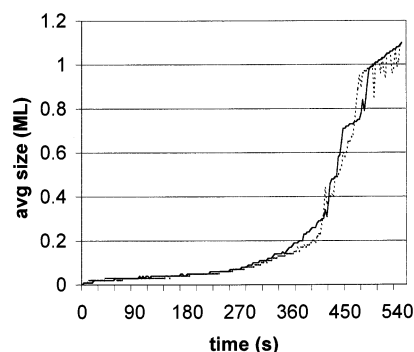
Figure 8. Average Ni island size (in monolayer units) vs time (in seconds) for Ni(110) epitaxy. The cases given are for 1.1 monolayers of Ni deposited over 550 s both with 0.05 monolayer precoverage of H as a catalyst (solid curve) and without any H (dashed curve).

Figure 9. Average second-tier Ni island size (in absolute number) vs time (in seconds) for Ni(110) epitaxy. The cases given are for 1.1 monolayers of Ni deposited over 550 s both with 0.05 monolayer precoverage of H as a catalyst (solid curve) and without any H (dashed curve).
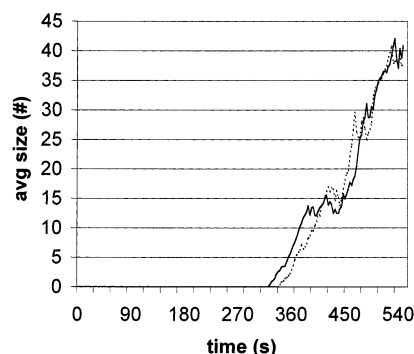
line). In the simulations of Figures 8 and 9, Ni adatoms are deposited at a 500 s/monolayer growth rate for 550 s, and a first point to note is the more limited effect of hydrogen on the overall island size as compared to the (100) surface. Over about the first 350 s of deposition (giving a total of 0.7 monolayer Ni deposited), notice from Figure 8 that stable second-tier islands are only beginning to form, and notice also the slow smooth growth of the average island size in Figure 8 rising to about 0.1 monolayer average size. This is the region in which the long thin islands are growing in length and more slowly in width, which we verify computationally by printing out timed snapshots of the KMC island patterns as they grow (Figure 10). From about 350−500 s, the single-layer islands become globally connected (as the Figure 8 curve rises quickly to approach a value near unity), and second-tier islands form (as Figure 9 shows a nearly steady rise representing the net effect of second-tier deposion and step-down mobility) as a full monolayer of Ni becomes deposited at 500 s.

For comparison, recall that on the Ni(100) surface, the 0.1 monolayer average island size appears at about 0.3−0.4 monolayer total deposition, or 150−200 s (depending on H catalysis) and that roughening (stable second-layer island formation) begins at this same time (0.3 monolayer). Recall also that the Ehrlich−Schwoebel step-edge barriers are not vastly different in magnitude for the (110) and the (100) surface. Nevertheless, using the same deposition rates for both surfaces, the (100) surface shows far more roughness than the (110) surface, as noted graphically by comparing Figures 3 and 9 at equal times. In the KMC simulations, this roughening distinction can be traced back to the greater lone-atom mobility on the (110) surface along with the short distances that a second-layer
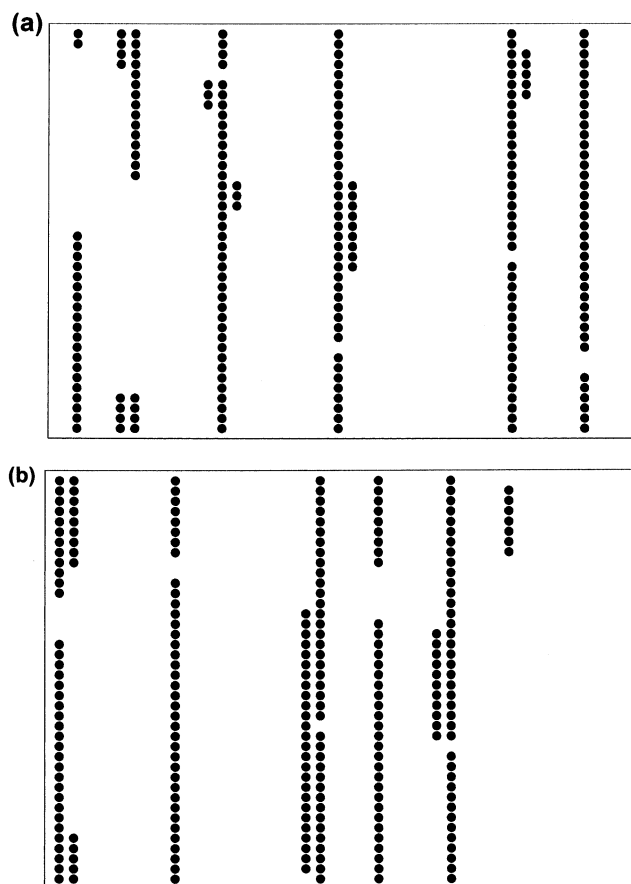

Figure 10. Typical sample of the second-layer growth pattern on Ni-(110) at the 1.1 monolayers coverage with (a) and without (b) H-atom catalysis on a 40 × 40 grid with periodic boundary conditions. The images corresponding to the data given in Figure 9 taken at the final time point and only the Ni atoms are shown.

atom need move in the long-axis direction to find a step edge (because the growth pattern involves those long narrow islands). We have tested this by artificially slowing the mobility of only the second-layer lone (110) atoms to match that of their (100) counterparts. In this test, we match the hopping energy barriers along the second-tier (110) short axis to match the hopping barrier of the (100) surface, and we also lower the hopping mobility by the same amount along the long axis to maintain the $x-y$ asymmetry in barrier height. The result of this test is a significant roughening in the (110) growth case, at approximately the level seen for the (100) case.

As generic samples of the actual surface patterns, "snapshot" images of a Ni(110) surface showing a typical growth pattern both with (Figure 10a) and without (Figure 10b) H-atom catalysis are given. The $x-y$ asymmetry in the figure corresponds to the asymmetry of the long versus short axis for this surface. These images correspond to the data in Figure 9; it is taken at the final time point and for clarity shows only the second-tier layer Ni atoms for the 1.1 monolayers deposition on a 40 × 40 grid (the first layer is about 95% filled). Unlike the Ni(100) case discussed above, for Ni(110) the growth pattern is essentially layer-by-layer, and the images given here for second-tier patterns are indistinguishable from those seen on the first layer when an equal number of atoms have been deposited. The long, thin island patterns for (110) growth, connected via the short distances found along the short-axis are clear here as well, and a number of kinks are still apparent as the surface continues to evolve. Very similar patterns have been reported in the literature for Ag(110) and Cu(110) cases.[48,49]

Effects of Hydrogen on Ni(100) and Ni(110) Homoepitaxy

J. Phys. Chem. B, Vol. 106, No. 43, 2002 **11261**

Also the lack of significant H-catalyzed morphology distinction in average island size and island number, as discussed above, is also clearly apparent. The H-catalyzed case (10a) shows 6 islands with an average size of 37 Ni atoms, and the uncatalyzed case (10b) shows 6 islands with an average size of 40 Ni atoms, in good agreement with Figure 9.

IV. Summary

We have calculated activation energies for a set of Ni hopping events representing the Ni adatom diffusion, island condensation, island evaporation, and island flattening upon a Ni(100) and Ni(110) substrate, with and without the effect of having a proximate H atom (as an impurity) upon the activation energies of the same Ni hopping events. The rate constants based upon these activation energies are then used to simulate homoepitaxial growth via KMC simulations, with up to 0.7 and 1.1 monolayers of growth, respectively, for the (100) and (110) surfaces.

On the Ni(100) surface, we use a total of 88 uncatalyzed rate constants (and 88 H-catalyzed ones) corresponding to a variety of terrace level and step edge mobilities. We find that the presence of highly mobile H atoms has measurable effects on the size and roughness of Ni islands. The H atoms can catalyze the formation of larger islands (as seen in Figure 2). The H atoms are also involved in catalyzing a variety of different effects regarding multilayer growth and roughening of the Ni-(100) surface, and the KMC studies show that the net effect of the H atoms is to accelerate the breakdown of 3-d Ni island features formed during the epitaxial growth (as seen in Figure 3). On the Ni(110) surface, we use a total of 224 uncatalyzed rate constants (and 224 H-catalyzed rate constants) corresponding to a variety of terrace level and step edge mobilities. A key distinction of the (110) surface as compared to the (100) surface is that either with or without the presence of H, the (100) surface growth shows much more extensive roughening than does the (110) surface (as seen in Figures 8−9) which shows essentially layer-by-layer growth. KMC studies trace this difference to the axis asymmetry in the (110) case, and in particular to the short vs long axis binding energy asymmetry, which also results in a growth pattern of long narrow islands. Also on the Ni(110) surface we find that the presence of highly mobile H atoms has very modest effects on both island formation and 3-d island character, due to a more limited catalytic effect.

V. Appendix

A. KMC Grid Size. We have tested the computational grid size for the KMC simulations by both increasing and decreasing the numbers of grid points in the (x, y) surface parallel directions, and by monitoring the number of atoms that occupy various growth levels in the z-direction (perpendicular to the surface). For the case of Ni(100), we have found that three layers in the z-direction are sufficient to accommodate the growth through the 0.7 monolayer regime examined in this report. At least a tetramer formation of third-layer Ni atoms would be required to form the base for a fourth layer, and in our simulations we almost universally found only monomers, and occasionally dimers forming on the third layer.

In the (x, y) directions, the KMC simulation relies on periodic boundary conditions and the consequence of an overly small (x, y) grid is that the artificial correlations which can arise between atoms leaving one side and reappearing on the other
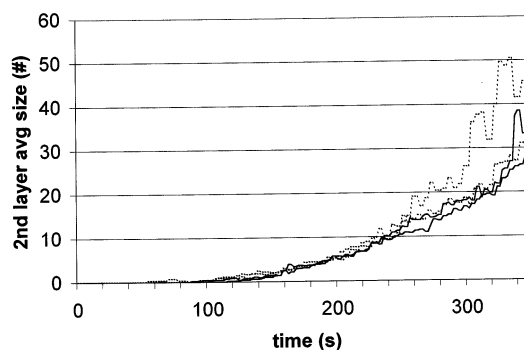

Figure 11. Average second-tier Ni island size (in absolute number) vs time (in seconds) for Ni(100) epitaxy to test various grid sizes. The cases given are for square grids of size 30 (upper dashed curve), 35 (upper solid curve), 40 (lower solid curve), and 50 (lower dashed curve).

may result in island patterns that are determined by the boundary conditions rather than by the kinetics of the simulation. In Figure 11 we examine some of these test results by focusing on the average absolute second-layer island size (which a key point of interest in the results section above), for square grids of 30, 35, 40, and 50 binding sites, using at least 10 simulation iterations per grid size to carry out the average. For better comparison, the typical standard deviation of the average from the KMC simulations in each case is about ±5−7 at a time of 300 s. The highest dashed curve in Figure 11 is for the 30 × 30 grid size and for times beyond about 250 s the average size of this grid begins to rise distinctly above the others. We attribute this to a boundary effect on the basis of an examination of the first growth layer (not represented in Figure 11), which shows that island consolidation on the 30 × 30 grid is occurring faster than on the larger grids. By examination of both first-layer and second-layer (as seen in Figure 11) growth, we see a convergence of absolute second-layer island size starting at around the 35−40 grid size, and we have used the 40 × 40 grid as our standard size for the results reported in the main body of this report. Similar tests, with similar results, have been carried out for the Ni(110) surface, and for computational simplicity, a 40 × 40 grid is used in this case as well.

B. Reference Rate Constant. We have tested the computational reference rate constant for the KMC simulations by both increasing and decreasing it in test case simulations. The effect of the reference rate constant is to set the clock unit time for the KMC simulation. Events occurring on a faster time scale than that given by the reference value will occur during each clock interval (but no more often), whereas events occurring at the reference time scale or on a slower time scale will occur in correct proportion to one another. With a finite reference time scale, we are therefore misrepresenting some events that occur on faster time scales than the reference. As long as the misrepresented events do not significantly impact the observables, then the stochastic procedure with a fixed clock time is valid. In our study, as long as the fast time events are mainly associated with peripheral diffusion, which shifts the island edge back and forth, rather than with evaporation/condensation events (and the two are not of course totally separable), then the island size information reported above will be unaffected by the misrepresented events. We therefore make an initial judgment regarding where to set the reference rate constant by inspection of the hopping barriers involved, but we need to test that cutoff value computationally to have a better measure of confidence in our final results. For the Ni(100) KMC simulation, there are a total of 88 uncatalyzed rate constants used, and the number of distinguishable uncatalyzed rate constants for the reference

TABLE 3: Average Island Size, and Island Size Distribution, vs Time (s) for Various Reference Potentials (V_{ref}, eV, Labeled as 45, 40, 35, 30, 25) for the Test Case Discussed in Appendix B[a]

time (s)	av island size[b] for each V_{ref}					island size distribution for each V_{ref}				
	45	40	35	30	25	45	40	35	30	25
0.0	2.6	2.7	2.7	2.7	2.6	1.2	1.1	1.0	1.0	1.1
0.1	4.9	5.2	5.3	5.2	5.4	4.2	4.7	4.3	4.8	4.9
0.2	5.7	5.7	6.1	5.8	6.3	4.2	4.2	4.1	4.4	4.4
0.4	6.6	6.9	6.8	6.5	7.3	3.9	4.0	3.7	4.3	4.0
0.6	6.8	7.3	7.3	7.2	7.4	3.8	3.7	3.8	3.8	4.4
0.8	7.3	7.6	7.8	7.7	7.6	3.6	3.8	4.2	4.0	4.7
1.0	7.4	8.1	8.2	8.2	7.9	3.3	3.9	4.1	4.0	4.8
1.2	7.9	8.3	8.5	8.3	8.4	3.9	4.5	4.7	4.5	4.9
1.4	8.1	8.6	8.7	8.7	8.8	3.9	4.7	4.8	4.7	5.2
1.6	8.5	9.1	8.9	8.7	8.8	4.2	4.8	4.6	4.8	5.5
1.8	8.8	9.1	9.2	9.1	8.8	4.3	5.0	5.0	4.9	5.5
2.0	8.9	9.0	9.3	9.4	8.8	4.6	5.1	5.0	5.0	5.5
k_{dist}	54	54	54	59	71					
N_{hops}	1.8(+2)	1.6(+3)	1.5(+4)	1.6(+5)	6.6(+5)[c]					

[a] Also given are the number of distinguishable uncatalyzed rate constants (k_{dist}) and the average number of adatom hops per adatom (N_{hops}) for each V_{ref}. [b] The standard deviation of the average island size increases from 0.2 at $t = 0.0$ s to a range of 0.5–1.1 at $t = 1.0$ s and to a range of 0.8–1.3 at $t = 2.0$ s for each of the cases. [c] This notation 6.6(+5) means $6.6 \times 10^{+5}$, for example.

energies $V_{ref} = 0.45, 0.4, 0.35, 0.3$, and 0.25 eV are given, noted as k_{dist}, in the second to last row of Table 3, where we see a range of 54 to 71 for the cases noted. Note that a plateau value of 54 distinguishable rate constants exists across the 0.45–0.35 eV range of V_{ref}, and for the catalyzed case these values are 50, 61, and 63, respectively, for the 0.45, 0.40, and 0.35 eV cases. These values suggest that a cutoff in the 0.4 eV range may be appropriate, and we carry out two computational studies to test this idea.

As a first test, we have started from an instantaneous deposition of 0.15 monolayer of Ni atoms on a Ni(100) 30 × 30 grid and carried out short time KMC dynamics to examine the initial small island condensation/evaporation for a variety of reference rate constants. This test magnifies the number of small island formation events due to the instantaneous 0.15 monolayer configuration. Because it is the small islands that have the largest circumference-to-area ratio, they proportionately have a great number of various corner and kink sites that are of importance in the peripheral diffusion processes that our standard results may misrepresent. In Table 3 we present the average island size and island size distribution (the standard deviation of the island size) at selected times over the $t = 0-2$ s range after the initial 0.15 monolayer deposition for several reference energy values, $V_{ref} = 0.45, 0.4, 0.35, 0.3$, and 0.25 eV. Ten KMC simulations for each reference energy were carried out and averaged together. Very similar island sizes and distributions are noted across this series, whereas the number of distinguishable rate constants, from Table 3, differs dramatically. Because the reference energy controls the time unit of the simulation, the number of adatom hopping events also changes dramatically during this test, and this is noted in the last row of Table 3, as the number of hops per adatom, denoted N_{hop}, where we see a range from 1.7×10^2 to 6.6×10^5. This suggests that many of the additional hops are simply shifts back and forth, or canceling out in some other manner. At a reference value of about 0.45 eV, a breakdown in the pattern is starting to appear, noted by both slightly smaller island sizes and size distributions (though only at the edge of statistical significance). A dramatic breakdown in this pattern occurs in the 0.5–0.52 eV reference energy range as progressively less and less adatom dynamics, and therefore island evolution, occurs, and the longer time values drift only slightly from the initial ($t = 0$) values. The result of this test suggests that a reference energy value of 0.4 eV appears reasonable.
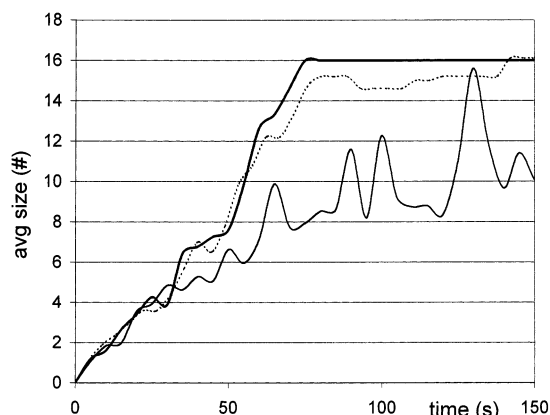

Figure 12. Average first-layer Ni island size (in absolute number) vs time (in seconds) for Ni(100) epitaxy to test various reference potentials. The cases given are for 0.10 monolayer Ni deposition occurring during the first 50 s, using a square grid of size 30, and with reference potentials of 0.45 eV (lower solid curve), 0.40 eV (dashed curve), and 0.30 eV (upper solid curve).

As a second test we examine the realistic deposition rate (500 s/monolayer) and growth time for a subset of these reference energy values, to better correspond to the parameters used in the main body results of this paper. This test is represented in Figure 12, where we indicate the first-layer average island size for 0.3 monolayer Ni(100) growth using a 30 × 30 grid size and several reference rate constants based on energy values of 0.3, 0.4, and 0.45 eV. For these three reference values the average number of hops per adatom over the full 150 s time noted are 1.9×10^6, 1.5×10^4, and 2.9×10^3, respectively, showing the dramatic change in number of hopping events. Even with the 2 orders of magnitude difference in the number of hops for the 0.3 and 0.4 eV reference energies, the observables are not dramatically different, whereas dramatic effects do accrue at the 0.45 eV level. On the basis of these test results, a value of 0.4 eV (as used for the final results reported in this report) appears reasonable.

Similar tests have been carried out on the Ni(110) surface and the results are similar (and even more conservative), which is not especially surprising because the effective ranges of energy barriers on the (100) and (110) surfaces are quite similar, but with the (110) surface having fewer low energy barriers. For example, out of a total of 224 rate constants used in the

Effects of Hydrogen on Ni(100) and Ni(110) Homoepitaxy

J. Phys. Chem. B, Vol. 106, No. 43, 2002 **11263**

Ni(110) KMC simulation, the reference energy value of 0.40 eV distinguished 211 of the rate constants. For consistency, we have therefore used the 0.40 eV reference energy value for the main body results given above for both Ni surfaces.

References and Notes

(1) Haug, K.; Zhang, Z.; John, D.; Walters, C. F.; Zehner, D. M.; Plummer, W. E. *Phys. Rev. B* **1997**, *55*, R10233−R10236.

(2) Haug, K.; Do, N. K. N. *Phys. Rev. B* **1999**, *60*, 11095.

(3) Haug, K.; Jenkins, T. *J. Phys. Chem. B* **2000**, *104*, 10017.

(4) Trevor, D. J.; Chidsey, C. E. D. *J. Vac. Sci. Technol. B* **1991**, *9*, 964.

(5) De la Figuera, J.; Pristo, J. E.; Ocal, O.; Miranda, R. *Solid State Commun.* **1994**, *89*, 815.

(6) Morgenstern, K.; Rosenfeld, G.; Poelsema, B.; Comsa, G. *Phys. Rev. Lett.* **1995**, *74*, 2058.

(7) Wen, J.-M.; Chang, S.-L.; Burnett, J. W.; Evans, J. W.; Thiel, P. A. *Phys. Rev. Lett.* **1994**, *73*, 2591.

(8) Hamilton, J. C.; Daw, M. S.; Foiles, S. M. *Phys. Rev. Lett.* **1995**, *74*, 2760.

(9) Van Siclen, C. DeW. *Phys. Rev. Lett.* **1995**, *75*, 1574.

(10) Khare, S. V.; Bartelt, N. C.; Einstein, T. L. *Phys. Rev. Lett.* **1995**, *75*, 2148.

(11) Sholl, D. S.; Skodje, R. T. *Phys. Rev. Lett.* **1995**, *75*, 3158.

(12) Voter, A. F. *Phys. Rev. B* **1986**, *34*, 6819.

(13) Stumpf, R. *Phys. Rev. Lett.* **1997**, *78*, 4454.

(14) Kellogg, G. L. *Phys. Rev. B* **1997**, *55*, 7206.

(15) More, S.; Berndt, W.; Bradshaw, A. M.; Stumpf, R. *Phys. Rev. B* **1998**, *57*, 9246.

(16) Khare, S. V.; Einstein, T. L. *Phys. Rev. B* **1998**, *57*, 4782.

(17) Huang, Y.-C.; Flidr, J.; Newton, T. A.; Hines, M. A. *Phys. Rev. Lett.* **1998**, *80*, 4462.

(18) Kellogg, G. L. *Phys. Rev. Lett.* **1998**, *79*, 4417.

(19) Bogicevic, A. *Phys. Rev. Lett.* **1999**, *82*, 5301.

(20) Tung, R. T.; Graham, W. R. *Surf. Sci.* **1980**, *97*, 73.

(21) Peale, D. R.; Cooper, B. H. *J. Vac. Sci. Technol. A* **1991**, *10*, 2210.

(22) Esch, S.; Hohage, M.; Michely, T.; Comsa, G. *Phys. Rev. Lett.* **1994**, *72*, 518.

(23) Vrijmoeth, J.; van der Vegt, H. A.; Meyer, J. A.; Vlieg, E.; Behm, R. J. *Phys. Rev. Lett.* **1994**, *72*, 3843.

(24) Oppo, S.; Fiorentini, V.; Scheffler, M. *Phys. Rev. Lett.* **1993**, *71*, 2437.

(25) Zhang, Z. Y.; Lagally, M. G. *Phys. Rev. Lett.* **1994**, *72*, 693.

(26) Copel, M.; Tromp, R. M. *Phys. Rev. Lett.* **1994**, *72*, 1236.

(27) Kellogg, G. L.; Plass, R. A. *Surf. Rev. Lett.* **2000**, *7* (5−6), 649.

(28) Thurmer, K.; Reutt-Robey, J. E.; Williams, E. D.; Uwaha, M.; Emundts, A.; Bonzel, H. P. *Phys. Rev. Lett.* **2001**, *87* (18), 186102.

(29) Montalenti, F.; Sorensen, M. R.; Voter, A. R. *Phys. Rev. Lett.* **2001**, *87* (12), 126101.

(30) Zhang, Z.; Chen, X.; Legally, M. *Phys. Rev. Lett.* **1994**, *73*, 1829.

(31) Amar, J. G.; Family, F. *Phys. Rev. Lett.* **1995**, *74*, 2066.

(32) Bartelt, M. C.; Evans, J. W. *Phys. Rev. Lett.* **1995**, *75*, 4250.

(33) Khare, S. V.; Bartelt, N. C.; Einstein, T. L. *Phys. Rev. Lett.* **1995**, *75*, 2148.

(34) Fichthorn, K. A.; Scheffler, M. *Phys. Rev. Lett.* **2000**, *84*, 5371.

(35) Daw, M. S.; Baskes, M. I. *Phys. Rev. B* **1984**, *29*, 6443.

(36) (a) Wonchoba, S. E.; Hu, W. H.; Truhlar, D. G. *Phys. Rev. B* **1995**, *51*, 9985. (b) Wonchoba, S. E.; Truhlar, D. G. *Phys. Rev. B* **1996**, *53*, 11222.

(37) Fichthorn, K. A.; Weinberg, W. H. *J. Chem. Phys.* **1991**, *95*, 1090.

(38) Liu, Y.-T.; Metiu, H. *Surf. Sci.* **1991**, *245*, 150.

(39) Uebing, C. In *Surface Diffusion: Atomistic and Collective Processes*; Tringides, M. C., Eds.; Plenum Press: New York, 1997.

(40) Eberhardt, W.; Greuter, F.; Plummer, E. W. *Phys. Rev. Lett.* **1981**, *46*, 1085.

(41) Rieder, K. H.; Stocker, W. *Phys. Rev. Lett.* **1986**, *57*, 2548.

(42) Behm, R. J.; Penka, V.; Cattania, M. G.; Christman, K.; Ertl, G. *J. Chem. Phys.* **1983**, *78*, 7486.

(43) Johnson, A. D.; Maynard, K. J.; Daley, S. P.; Yang, Q. Y.; Ceyer, S. T. *Phys. Rev. Lett.* **1991**, *67*, 927.

(44) Go, E. P.; Thuermer, K.; Reutt-Robey, J. E. *Surf. Sci.* **1999**, *437*, 377.

(45) Ehrlich, G.; Hudda, F. G. *J. Chem. Phys.* **1966**, *44*, 1039. Ehrlich, G. *Surf. Sci.* **1994**, *299/300*, 628.

(46) Schwoebel, R. L.; Shipsey, E. J. *J. Appl. Phys.* **1966**, *37*, 3682.

(47) Tsong, T. T. In *Surface Diffusion: Atomistic and Collective Process*es Tringides, M. C., Ed.; Plenum Press: New York, 1997.

(48) Ferrando, R.; Hontinfinde, F.; Levi, A. C. *Phys. Rev. B* **1997**, *56*, R4406.

(49) Mottet, C.; Ferrando, R.; Hontinfinde, F.; Levi, A. C. *Surf. Sci.* **1998**, *417*, 220.

(50) Kellogg, G. L.; Feiblemann, P. J. *Phys. Rev. Lett.* **1990**, *64*, 3143.

(51) Feiblemann, P. J. *Phys. Rev. Lett.* **1990**, *65*, 729.